


RESEARCH PAPER OPEN ACCESS

Molecular Dynamics Simulations of a Putative Novel Mechanism for UCP1-Assisted FA Anion Transport

Sanja Vojvodić¹ | Giorgia Roticianni¹ | Mario Vazdar² | Elena E. Pohl¹ 

¹Physiology and Biophysics, Department of Biological Sciences and Pathobiology, University of Veterinary Medicine, Vienna, Austria | ²Department of Mathematics, Informatics, and Cybernetics, Faculty of Chemical Engineering, University of Chemistry and Technology, Prague, Czech Republic

Correspondence: Sanja Vojvodić (sanja.vojvodic@vetmeduni.ac.at) | Mario Vazdar (mario.vazdar@vscht.cz) | Elena E. Pohl (elena.pohl@vetmeduni.ac.at)

Received: 17 September 2024 | **Revised:** 2 May 2025 | **Accepted:** 22 May 2025

Funding: This project was supported by the Horizon 2020 Research and Innovation Program of the European Union under Marie Skłodowska-Curie Grant Agreement No. 860592 (to E. E. P.). M. V. acknowledges support from the Ministry of Education, Youth and Sports of the Czech Republic through the e-INFRA CZ (ID:90254), Project OPEN-30-53. The authors would like to acknowledge networking support by the COST Action CA21169 (European Cooperation in Science and Technology). We thank the Vienna Scientific Cluster (VSC) for computational resources. Open Access is funded by the University of Veterinary Medicine Vienna.

Keywords: anion transporter | cardiolipin | fatty acid cycling | mitochondrial SLC25 family | molecular dynamics simulations | proton transport mechanism

ABSTRACT

Background: Mitochondrial energy can be stored as ATP or released as heat by uncoupling protein 1 (UCP1) during non-shivering thermogenesis in brown adipose tissue. UCP1, located in the inner mitochondrial membrane, reduces the proton gradient in the presence of long-chain fatty acids (FA). FA act as weak, protein-independent uncouplers, with the transport of the FA anion across the membrane being the rate-limiting step. According to the fatty acid cycling hypothesis, UCP1 catalyzes this step through an as-yet-undefined mechanism.

Methods: We used computational and experimental techniques, including all-atom molecular dynamics (MD) simulations, membrane conductance measurements, and site-directed mutagenesis.

Results: We identified two novel pathways for fatty acid anion translocation (sliding) at the UCP1 protein–lipid interface, ending at key arginine residues R84 and R183 in a nucleotide-binding region. This region forms a stable complex with fatty acid anion, which is crucial for anion transport. Mutations of these two arginines reduced membrane conductance, consistent with the MD simulation prediction that the arachidonic acid anion slides between helices H2–H3 and H4–H5, terminating at R84 and R183. Protonation of the arachidonic acid anion predicts its release from the protein–lipid interface, allowing it to move to either cytosolic or matrix leaflets of the membrane.

Conclusion: We provide a novel, detailed mechanism by which UCP1 facilitates fatty acid anion transport, as part of the fatty acid cycling process originally proposed by Skulachev. The residues involved in this transport are conserved in other SLC25 proteins, suggesting the mechanism may extend beyond UCP1 to other members of the superfamily.

1 | Introduction

The complex machinery of electron transport chain proteins in the inner mitochondrial membrane (IMM) triggers the

formation of the transmembrane proton gradient. The chemiosmotic hypothesis proposes that the proton gradient across the IMM causes oxidative phosphorylation, i.e., the synthesis of the energy unit—adenosine triphosphate (ATP)—in

This is an open access article under the terms of the [Creative Commons Attribution-NonCommercial-NoDerivs](https://creativecommons.org/licenses/by-nc-nd/4.0/) License, which permits use and distribution in any medium, provided the original work is properly cited, the use is non-commercial and no modifications or adaptations are made.

© 2025 The Author(s). *Acta Physiologica* published by John Wiley & Sons Ltd on behalf of Scandinavian Physiological Society.

respiring cells [1]. Protons can pass through the IMM, uncoupling the proton gradient from oxidative phosphorylation and allowing for the adjustment of energy metabolism to maintain and regulate metabolic homeostasis, non-shivering thermogenesis, carbon flow, and nutrient supply. The proton leak can be basal or regulated [2]. The basal leak is always present due to the slow spontaneous diffusion of hydrated protons (H_3O^+) across the membrane. The regulated leak is controlled by mitochondrial inner membrane proteins. Besides uncoupling protein 1 (UCP1), several other proteins of the SLC25 family have been reported to transport protons, such as the uncoupling proteins 2–5 (UCPs) [3], adenine nucleotide translocase (ANT1, also known as ADP/ATP carrier, AAC) [4–6] and oxoglutarate carrier (OGC) [7].

UCP1 is found in brown adipose tissue and regulates non-shivering thermogenesis by dissipating proton gradient energy as heat in the presence of long-chain fatty acids (FA) [8–10]. The process is inhibited by purine nucleotides, as shown in mitochondria [11, 12], mitoplasts [13], and using recombinant UCP1 reconstituted in liposomes or planar bilayer membranes [14–16].

The detailed molecular mechanism of the proton transport in the presence of UCP1 and FA remains unclear. Generally, two main pathways for protons have been proposed: (i) protonated FA carries a proton, while UCP1 transports the FA anion to complete the cycle (the FA cycling hypothesis [17, 18]) (Figure 1a) or (ii) a proton is transported through the central gate of UCP1, assisted by FA carboxyl groups (the FA buffering [19] or FA shuttling [13] models). In the buffering model, “UCP1 functions as an H^+ transporter with a channel for H^+ in which FA with its carboxyl provides an essential H^+ buffering or transferring group.” [20] In the shuttling hypothesis, the FA head is proposed to swing back and forth in the anionic or protonated state, transporting H^+ across the membrane to the matrix side [13]. In this scenario, the FA anion binds at the bottom of a protein cavity on the cytosolic side. UCP1 is thought to act “as a symporter that transports one long-chain FA and one H^+ per transport cycle, keeping the anion associated with

UCP1” [13]. However, the unlikelihood of this mechanism is underscored by the water-impermeable nature of the protein structure and the high positive electrostatic potential in the protein cavity, which has been calculated for the homologous AAC1 [21]. Electrostatic analysis of the trajectories involved in the observed spontaneous binding of ADP to AAC1 revealed that the electrostatic potential can reach the value of 1.2 V. This electrostatic potential appeared to be the primary driving force for nucleotide binding. Two distinct regions of charged residues in the AAC were identified as responsible for the formation of this electrostatic field. The first region includes residue R235 from the RRRMMM signature motif and a salt bridge ring composed of E29, K32, D134, R137, D231, and R234. The second region, a few angstroms above the first, includes residues K22, R79, and R279. Wang and Tajkhorshid suggested that the strong positive electrostatic potential is a common feature of the entire mitochondrial carrier family. This high electropositivity within the mitochondrial carrier cavity and the impermeability of the protein cast doubt on the idea that positively charged protons move easily through the cavity.

The FA cycling model (Figure 1a) [17, 18, 22] proposes that protonated FA first crosses the IMM and deprotonates at the matrix side, guided by the pH gradient and its apparent pK_a of ~ 7 [23, 24]. In the next step, the protein catalyzes the transport of the FA anion across the IMM back to the cytosolic side by an unknown mechanism (Figure 1a). The translocation of a neutral FA across the membrane takes place in a millisecond time range [25] with calculated translocation energy of $\sim 3 \text{ kcal mol}^{-1}$ for various saturated FAs [23]. We previously suggested that proton transport in ANT1 can be described by this hypothesis [5] and proposed the protein-associated sliding pathway for the translocation of FA^- [26]. Because crucial amino acid residues are conserved in the proteins of the SLC25 family [6, 27], including UCP1, we hypothesized that the pathway for FA anion movement along the protein may also be conserved.

In this study, we aimed to elucidate the mechanistic steps of FA anion upon translocation from the matrix to the cytosolic side of

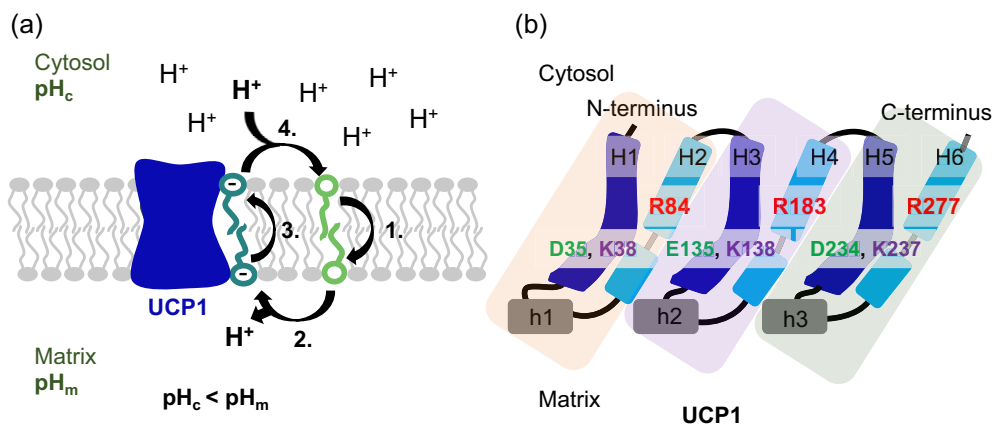


FIGURE 1 | Proton transport mechanism and structural basis in UCP1. (a) Original FA cycling model, neutral FA is shown in green, while the anionic form is shown in cyan. The model can be divided into four steps: 1. Translocation of protonated FA across the bilayer from the cytosolic to the matrix side; 2. Deprotonation of FA at the matrix side; 3. UCP1-assisted FA^- translocation; 4. Protonation of FA^- . (b) Schematic representation of the tripartite structure of UCP1. Each of the three subunits contains two long transmembrane helices (H1-H2, H3-H4, H5-H6) and one short perpendicualar helix (h1, h2, h3) at the matrix side.

the membrane at the UCP1–lipid interface. Based on the pseudo-threefold symmetry of UCP1, on MD simulations, and on a comparison of the conductance of the membranes reconstituted with UCP1 and its critical mutant, we proposed two possible pathways for the translocation of FA anions.

2 | Results and Discussion

2.1 | Modeling of UCP1

UCP1 is a monomer with a size of ~32 kDa. The tertiary structure of human UCP1 was recently solved using cryo-electron microscopy (cryo-EM) in its substrate-free state [28] and in complex with ATP, DNP [28], or GTP [29]. We have first shown that alignment between the UCP1 structure based on the AlphaFold mouse structure (AF-P12242-F1-v4) [30] and the nucleotide-free structure open to the cytosolic side (c-state) is valid, especially in the crucial central cavity of the protein (Figure S1). The root mean square deviation (RMSD) of the two structures (1.57 Å) is smaller than the resolution of the UCP1 cryo-EM structure in its substrate-free state (8HBV, resolution 2.51 Å) [28].

2.2 | MD Simulations of UCP1 in the Presence of Cardiolipin and Arachidonic Acid Show Stability of UCP1 Over Time

As the activity of the protein depends on the lipid properties [31,32], we simulated the Alpha Fold (AF) UCP1 structure in a DOPC:DOPE bilayer with three cardiolipins (CLs) bound at the UCP1 matrix side [33], which corresponds to the physiological lipid membrane composition in mitochondria. We simulated the system with and without the addition of arachidonic acid in both protonated (AA) and anionic (AA⁻) forms, initially positioned in both leaflets of the bilayer. The RMSD shows that both systems were stable and equilibrated in time (Figure S2a), with slightly more oscillations in the system with AA/AA⁻. Fluctuations along the protein (Root Mean Square Fluctuation, RMSF) for both systems showed higher flexibility in loop regions and regions exposed to water and less flexibility in the transmembrane regions (Figure S2b). The analysis suggests a valid initial protein structure and systems that are stable over time.

2.3 | A Positively Charged UCP1 Matrix Ring Binds Cardiolipin

The structure of UCP1 is pseudo-threefold symmetric with three repeating units. Each unit consists of two long transmembrane alpha helices and a short perpendicular alpha-helix on the matrix side that connects the long helices. UCP1 has six long helices (H1–H6) and three short helices (h1–h3) (Figure 1b). The analogous helices have repeating motifs. Each of the odd-numbered helices (H1, H3, and H5) has a pair of positively and negatively charged amino acids that together form a salt bridge network that prevents water leakage (H1-D35—H3-K138, H5-D234—H1-K38, H3-E135—H5-K237). The even-numbered helices (H2, H4, and H6) have three nucleotide-binding arginines (R84, R183, and R277) immediately above the salt bridge network (Figure 1b).

Positively charged amino acids on the matrix side, not involved in CL binding (Figure 2a) can attract deprotonated FA diffusing laterally along the lipids (Video S1). The positively charged matrix ring represents all positively charged residues (arginines and lysines) located on the matrix side of the protein (Figure 2b). The ring consists of 13 positively charged amino acids—seven lysines (residues K56, K67, K73, K151, K175, K261, K269) and six arginines (residues R40, R54, R140, R153, R162, R239). There are only four negatively charged residues on the matrix side, all of which are glutamic acids (E46, E69, E168, E262). The matrix side of the protein has a total charge of +9. It is therefore not surprising that during MD simulations, three negatively charged CLs are bound to the matrix side of the protein, maintaining its structure. Their position between the short helices h1, h2, and h3 perpendicular to the long transmembrane helices is stable during the 2 μs simulation (Figure 2a). These positions are consistent with recently published cryo-EM structures. In three cryo-EM structures (substrate-free state and in complex with ATP and DNP) [28] only one of the three CL positions was localized, whereas in the UCP1 complex with GTP [29] all three CLs were localized between the short perpendicular helices h1, h2, and h3 as in the above simulations. While the area between the short perpendicular helices is occupied by CLs, positively charged residues on the short helices h1 (K67), h2 (R162), and h3 (K261) are free to attract negatively charged fatty acid anions (Figure 2b). The calculated average electrostatic potential of UCP1 in the DOPC:DOPE bilayer with three bound CLs is also positive at h1, h2, and h3 (Figure 2c). This supports the UCP1 cryo-EM structure with positive patches on the UCP1 matrix side [28].

2.4 | Sliding of AA Anions Is Based on the Pseudo-Threefold Symmetry of UCP1

Based on the above and in accordance with the pseudo-threefold symmetry, FA anion sliding can only occur along the interface between lipids and parallel transmembrane helices that are not connected on the matrix side, namely, H2–H3, H4–H5, and H6–H1 (Figure 3a). In addition, the central core of the protein has a positive potential, which can be the driving force from the initially bound AA⁻ sliding to the positively charged matrix ring of the central cavity (Figure 2c; Figure S3), shown also in the cryo-EM structure of UCP1 [28]. That the binding of FA to the matrix side of UCP1 is a key interaction for proton transport was confirmed experimentally by NMR at the H1–H6 interface, where the carboxylate group of FA interacts with the basic residues near the matrix side of UCP1 [34]. Sliding is completed when the AA⁻ head group approaches the cytosolic water in the protein cavity, where it can be protonated. In UCP1, water is already present above the salt bridge network (Figure 3b). We assume that the three arginines (R84, R183, and R277) immediately above the salt bridge network are the final sites of AA⁻ sliding (Figure 3b). At this position, the AA⁻ head group is solvated from the cytosolic side and capable of protonation (Figure S5). Theoretically, AA⁻ can slide along three protein–lipid interfaces (Figure 3a) following one of three possible paths from three initial binding positions: (i) matrix h1, sliding along H6–H1 and ending at R277; (ii) matrix h2, sliding along H2–H3 and ending at R84; and (iii) matrix h3, sliding along H4–H5 and ending at R183.

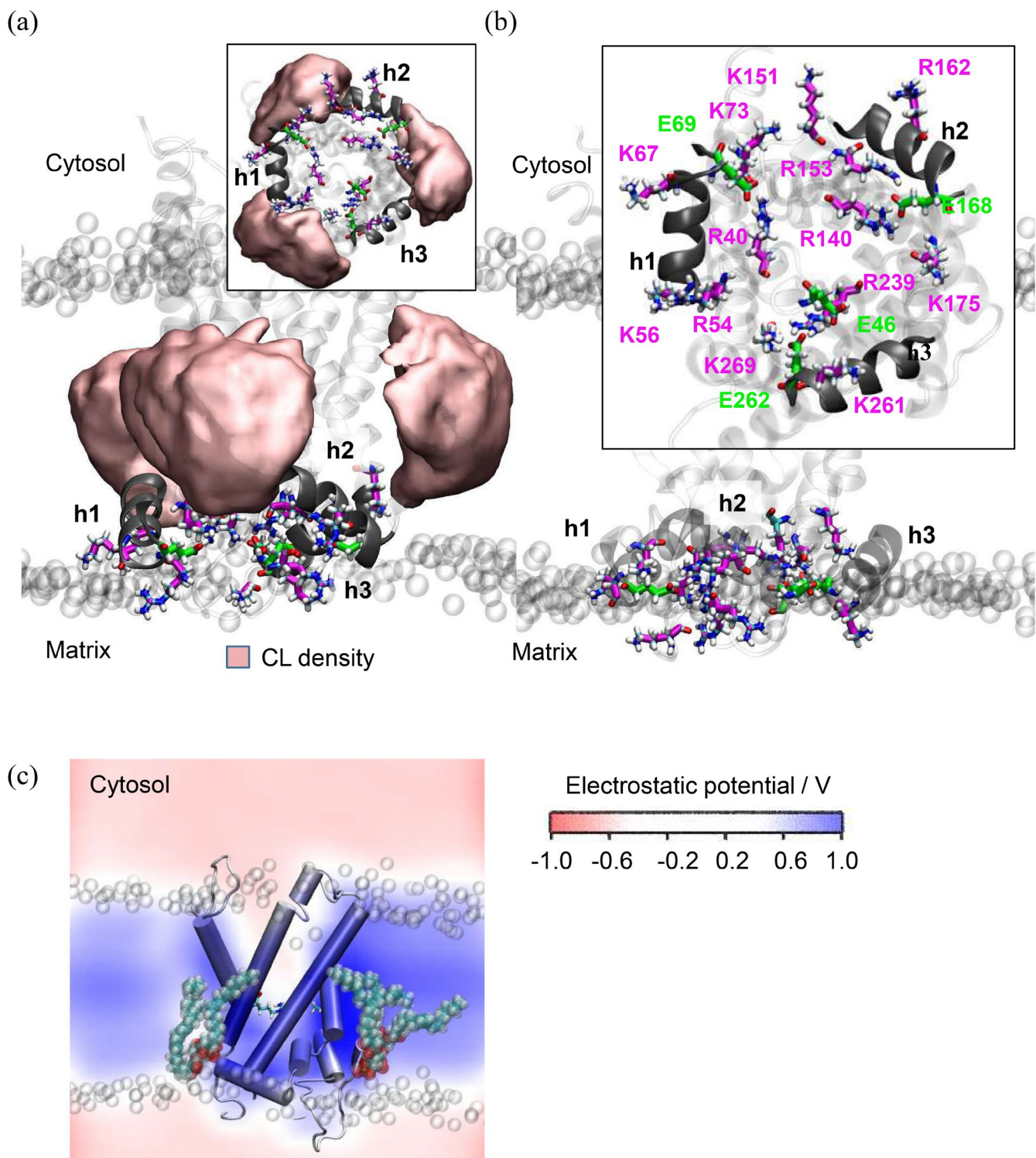


FIGURE 2 | Positively charged UCP1 binds three stabilizing cardiolipins (CLs) on the matrix side. (a) Average density of three CLs after a 2 μ s simulation bound to the protein between h1, h2, and h3 on the matrix side. All positively charged residues on the matrix side are shown in magenta, while all negatively charged residues are shown in green. (b) Side and matrix view (boxed) of positively charged residues shown in magenta and negatively charged residues (Glu) shown in green on the matrix side. (c) Averaged electrostatic potential along the x-plane. Protein is shown in the cartoon, CL molecules in vdW, and arginines from the arginine triplet in licorice. Headgroup atoms (N, P) of lipids are shown in vdW ghost.

MD simulations with neutral (AA) and anionic (AA⁻) forms of arachidonic acid, initially positioned in the lipid bilayer, showed that AA⁻ occupied only two of the proposed three matrix side hotspots between CL binding sites—the short perpendicular helices h2 and h3, but not the h1 (Figure 3c,d).

To test the MD simulations experimentally, we mutated the three central arginines to serines (R84S, R277S, and R183S) at the end of the putative sliding pathway. Membranes reconstituted with the mutants R84S and R183S had a lower conductance than the wild type, whereas mutation of R277 had

no effect on the conductance (Figure 3e; Figure S4). Mutation of R84 or R183 alone reduced conductance to 50%, but never completely abolished it (Figure 3e; Figure S4). We thus suggest that there are two possible sliding paths—(ii) H2–H3 ending in R84, and (iii) H4–H5 ending in R183—and when one of them is blocked, the other may still function. We have previously shown that the R79S mutant of ANT (analogous to R84S in

UCP1) has a 70% decrease in conductance, although conductance is not completely abolished [26]. This implies that the pathways along helices H2–H3 and H4–H5 ending in R84 and R183 could be involved in AA[−] sliding. The third pathway along helices H6–H1 ending at R277 does not seem to occur, probably because helices H6 (C-terminus) and H1 (N-terminus) are out of symmetry and have two (of four) negatively charged

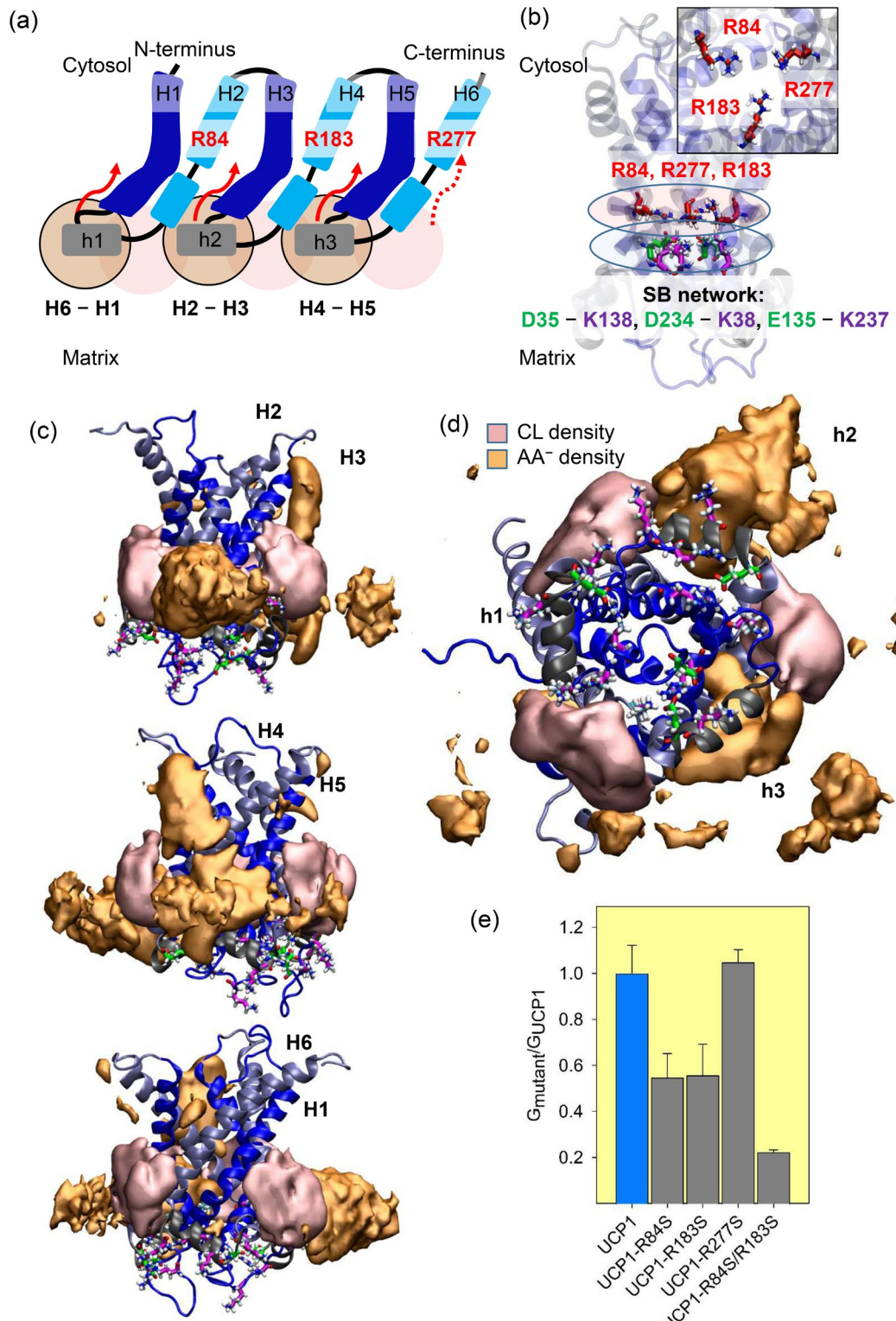


FIGURE 3 | Legend on next page.

FIGURE 3 | Sliding paths based on pseudo-threefold symmetry starting with the binding of AA⁻ on the matrix side between CLs and ending at the arginine triplet. (a) Schematic representation of the pseudo-threefold symmetry of UCP1. Pink transparent circles on the matrix side are CL binding sites (between h1, h2, and h3), and orange transparent circles are predicted AA⁻ binding sites (h1, h2, and h3). Red arrows are predicted sliding paths based on UCP1 symmetry starting from h1, h2, and h3 from the matrix side. (b) Salt bridge network (negatively charged residues included in the salt bridge in green, positively charged residues in purple) and nucleotide-binding arginine triplet in red. (c) Side view and (d) matrix side view for the average density of AA⁻ and CL in a 2 μ s MD simulation. The ratio of total membrane conductance, G_{mutant} , of membranes reconstituted with UCP1 mutants (UCP1-R84S, UCP1-R183S, UCP1-R277S) and the double mutant UCP1-R84S/R183S (e) to wild-type UCP1 of the membrane reconstituted with UCP1 in the presence of AA in the membrane. In all experiments, membranes were prepared from DOPC:DOPE:CL (45:45:10 mol%) and reconstituted with 15 mol% AA. The lipid concentration was 1.5 mg/mL and the protein concentration was 4 μ g/(mg lipid). The buffer solution consisted of 50 mM Na₂SO₄, 10 mM Tris, 10 mM MES, and 0.6 mM EGTA at pH = 7.34 and $T = 32^{\circ}\text{C}$. Data are the mean \pm SD of at least three independent experiments.

residues on the matrix side (Figure S6a)—glutamic acids E46 on H1 and E262 on H6. These negatively charged amino acids have a repulsive effect on the initial binding of negatively charged AA on the matrix side, thus preventing sliding toward R277. In addition, terminal R277 (H6) interacts with the negatively charged aspartate D28 (H1) (Figure S6b), which is located between R183 (D28–R183 center of mass average distance 1.50 ± 0.07 nm) and R277 (D28–R277 center of mass average distance 0.74 ± 0.05 nm), while two other terminal arginine residues (R84 and R183) are free to bind the AA⁻.

Path (iii) involving R183 is further supported by MD simulations showing the accumulation of AA⁻ around matrix h3 (Figure 3c,d) and direct spontaneous sliding along the protein helices H4–H5 (Figure 4; Video S1), and by mutation experiments (Figure 3e; Figure S4). The accumulation and initial binding of AA⁻ around h2 (path ii), together with the decrease in membrane conductance measured in bilayers reconstituted with the R84S mutant, suggests sliding along the protein helices H2–H3 in the pathway (ii). In the homologous ANT1, this pathway is confirmed by the spontaneous sliding of AA⁻ to arginine R79 (analog of R84 in UCP1, Figure 9) between helices H2–H3 [26]. Only pathway (i) ending at R277 does not seem promising for AA⁻ sliding, as there are not as many AA⁻ around h1 despite the positive electrostatic potential in the vicinity (Figure S3) and the R277S mutation shows no changes in conductance (Figure 3e; Figure S4). This pathway differs from the other two, as the terminal R277 is in contact with D28, and AA sliding should occur between helices H6–H1, the C-, and N-terminal helices with two glutamic acids on the matrix side. The latter interferes with the initial binding of the anionic head group of AA⁻. Based on our results, indicating that FA⁻ sliding occurs through two primary pathways terminating at R84 and R183, we produced a double mutant (R84S/R183S) (Figure 3e; Figure S4) to test whether blocking both pathways would completely abolish UCP1 activation. Our results showed a decrease in activation of more than 80%, indicating that these two pathways are the main routes for FA⁻ sliding. The incomplete loss of conductance upon double mutation could be due to the capacity for FA anion transport, potentially through minor alternative interactions or structural adaptability. The presence of residual conductance could also be due to the dynamic nature of membrane proteins, where local rearrangements in lipid–protein interactions could partially compensate for the loss of the two dominant pathways, maintaining a low level of conductance. Overall, our results strongly support the model in which the primary FA anion sliding pathways involve R84 and R183, with R277 playing no functional role.

2.5 | Sliding of AA⁻ Along the Protein–Lipid Interface From the Matrix Side Into the Protein Cavity

In a 2 μ s MD simulation, one of the AA⁻ spontaneously slides between helices H4 and H5 from the short perpendicular matrix h3 to arginine R183. In this case, spontaneous sliding is observed in an unbiased all-atom MD simulation. It is not a slow event (about 50 ns), but rather a rare event with a low probability that cannot be observed in all MD simulations on the microsecond time scale. The translocation is likely to be observed more frequently in MD simulations on millisecond or even longer timescales, which are unfortunately impossible to perform with current computational power. To increase the probability of the rare FA anion sliding, 10% AA (anionic and neutral form) was added to the studied system.

This confirms pathway (ii) as the sliding pathway (Figure 4). It implies a very low energy barrier for the UCP1-assisted translocation of anionic AA during sliding along the protein–lipid interface, compared to the known high energy of translocation of AA⁻ across the lipid bilayer (~ 16 kcal/mol) [23]. During the translocation process, the anionic head group of the AA⁻ is first attracted to the positively charged lysine K261 on the short helix h3 of the matrix side (Figure 4, 764 ns). The AA⁻ remained near h3 for about 50 ns and then jumped via lysine K237 (814 ns) to arginine R183 (Figure 4, 815 ns). In this final stable position, when bound to R183 and K237, the AA⁻ was located for more than 1000 ns until the end of the 2000 ns simulation (Figures 4 and 5). The AA⁻ is stabilized in two ways: (i) its hydrophobic tail—by lipids and hydrophobic amino acids and (ii) its negatively charged head group—by R183 and K237 (Figure 5).

Within a 5 Å radius around the AA⁻ head group, there are two negatively charged amino acids, E135, and D234 (Figure 4, zoom). The negative charge in the cavity contributes to local negative positions that can attract H₃O⁺, increasing the possibility of protonation of AA⁻.

The sliding pathway of the AA anion involves a rapid crossing of lysine 237. K237 is included in the salt bridge with E135, which is part of the salt bridge network that prevents water leakage (Figures 3b and 6a,b). As the K237–E135 salt bridge is disrupted and oscillates in time (Figure 6c,d), we calculated the average water volume and number density. The involvement of K237 does not significantly disturb the protein structure, and the protein cavity is still impermeable to water (Figure 6a,b,e).

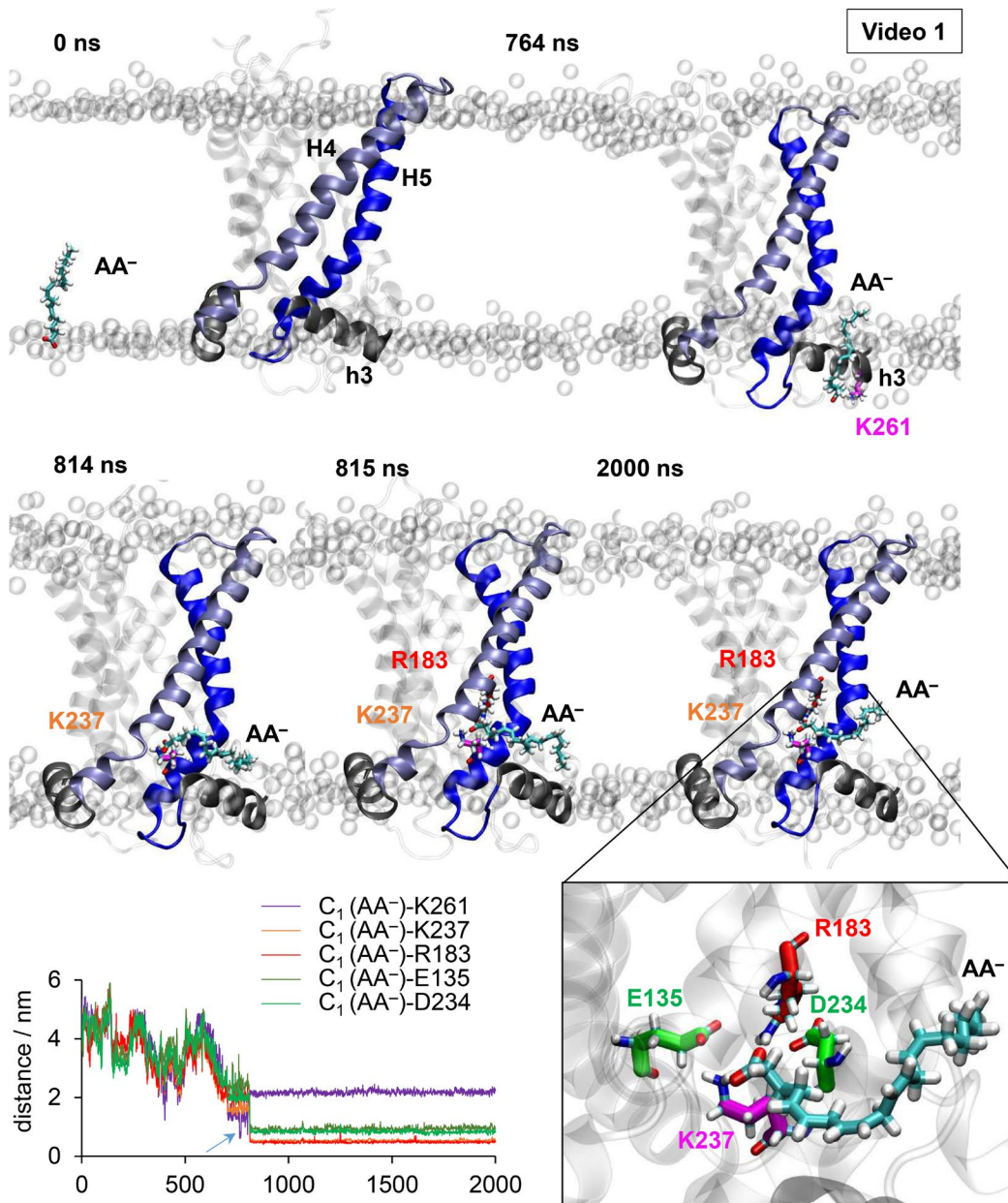


FIGURE 4 | Spontaneous sliding of AA⁻ between H4 and H5 of UCP1 was observed in an MD simulation. Timeline of the spontaneous sliding of AA⁻ in the 2 μs MD simulation. Zoom: 5 Å radius bound AA⁻ to R183 and K237 at $t=2\mu\text{s}$ in the vicinity of E135 and D234. The graph shows the distances between the C₁ atom of AA⁻ and the center of mass of the participating amino acids (K261, K237, and R183) and the surrounding negatively charged amino acids E135 and D234 when AA⁻ is bound to R183 and K237. The blue arrow indicates the attraction to K261 (approximately 764 ns). See also Video S1 in Supplementary Results.

2.6 | The Neutral Form of AA Spontaneously Exits the Protein–Lipid Interface Into the Bilayer

To see how the AA behaves in its neutral form, we protonated the anion at the end of the simulation ($t=2000\text{ ns}$). Since the protein is open to the cytosolic side (Figure 6a,b), water together with H₃O⁺ protrudes from the cytosolic side and can protonate the bound AA anion. Figure 7 shows that the protonated AA head group exits the protein cavity in less than 50 ns, while the hydrophobic tail is stabilized by the hydrophobic surface of the protein from one side and the hydrophobic tails of the lipids from the other side (Figures 5 and 7, Video S1). After 710 ns, the protonated AA tail leaves the protein interface and enters the matrix

lipid leaflet (Figure 7, 720 ns). There is an equal probability for the neutral form to exit the cavity to the cytosolic leaflet due to the low energy barrier for the flip-flop of protonated FA [23, 25].

2.7 | Modification of the Proton Transport Mechanism in UCP1 According to MD Simulation Results

The new results allow us to propose a modified FA cycling mechanism. The first two steps, translocation (step 1 in Figure 8) and deprotonation (step 2 in Figure 8) on the matrix side, are unchanged. After translocation and deprotonation, the FA⁻, can

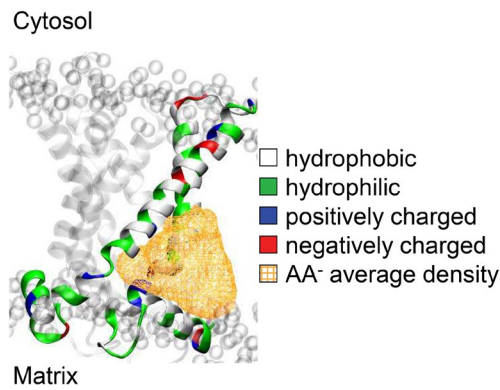


FIGURE 5 | Stabilization of AA^- at the protein–lipid interface. Average AA^- density when bound to R183, 815–2000 ns time range. UCP1 secondary structure of long transmembrane helices H4 and H5 and matrix short helices h2 and h3 are colored according to residue type.

be attracted to three positively charged matrix-side patches on short perpendicular helices of the matrix (h1, h2, and h3) and can slide to the cytosolic side (step 3 in Figure 8). Based on MD simulations and electrophysiological experiments, there are two possible pathways starting from (ii) matrix h2, sliding along H2–H3 and ending at R84, and (iii) matrix h3, sliding along H4–H5 and ending at R183. When the terminal arginines (R84 and R183) are reached, the carboxyl head group of the FA anion is solvated and can be protonated in the protein cavity by H_3O^+ in water coming from the cytosolic side. After protonation, the neutral FA is released toward the matrix or cytosolic side of the bilayer (step 4 in Figure 8). If the FA is released toward the matrix side of the bilayer, the first step in the next cycle is skipped and the entire cycle is shortened by one step. If FA is released to the cytosolic side, the whole cycle starts again from the first step. The final destination of the FA after detachment depends on the interplay between the concentration gradients of fatty acid and proton across the membrane. If a proton gradient exists such that the pH in the cytosol is lower than in the matrix ($\text{pH}_{\text{cytosol}} < \text{pH}_{\text{matrix}}$), there will be a higher concentration of protonated FA at the cytosolic leaflet of the bilayer. These protonated FA are likely to move directly to the matrix side of the leaflet to reach equilibrium, driven by the excess of FA anions on the matrix side.

2.8 | Generalization of the Mechanism to Other Proteins in the SLC25 Carrier Family

Conductance measurements suggest that other mitochondrial carriers in the SLC25 superfamily, such as UCP2-5, ANT1, and OGC, have the same ability to be activated by FA [5, 7, 35]. We thus propose that the FA sliding mechanism can be generalized to other proteins in the SLC25 superfamily, as UCP1 has highly conserved amino acids that are included in the proposed pathway of FA^- (Figure 9). The arginine triplet (R84–H2, R183–H4, and R277–H6) at the end of the sliding pathway is highly conserved in all the proteins mentioned [7]. ANT1 represents an exception: the arginine triplet is not symmetrically distributed/conserved in the even-numbered helices H2, H4, and H6 as in other proteins, and an arginine at H4

is replaced by a lysine at H1. ANT1 has K/R at H1, H2, and H6 (K22–H1, R79–H2, and R279–H6). This is unique to ANT1 as an ADP/ATP carrier. In contrast, for other members of the SLC25 family, ATP and ADP act as inhibitors. Also conserved is the matrix-forming salt bridge network (c-state of the protein) at helices H1, H3, and H5 and the proline kinks at odd-numbered helices (H1, H3, and H5), positioned two residues before the negatively charged amino acids (D/E) that form the salt bridge (Figure 9a). UCP1, UCP2, and UCP3 have the highest degree of conservation with an identity higher than 50%, with UCP2 and UCP3 being 75% identical (Figure 9b). ANT1 has the lowest identity with all proteins compared (between 20% with UCP1 and 26% with UCP5).

2.9 | Conclusion

Our study is the first to propose and provide a detailed molecular-level explanation of the proton transport mechanism in UCP1, specifically through the transport of the FA anion in a cycling process. In the mechanism of FA cycling without protein, FA^- anion transport is the bottleneck. We have shown that UCP1 can catalyze this step and that the FA^- anion slides along the protein–lipid interface between helices H4 and H5. The FA^- initially binds to K261 on the matrix side and slides via K237 to one of the nucleotide-binding sites, R183. Although K237 is part of the salt bridge network and water is disrupted on the H4–H5 matrix side, the protein remains impermeable. FA^- anion binding to R183 is stable, cytosolic water is accessible, and the FA^- anion can be protonated. Two negatively charged residues (E135 and D234) are nearby and can attract protons to this region of the protein cavity. Once protonated, the FA head group exits the protein interior and is released into lipids within 700 ns.

Based on the pseudo-threefold symmetry, we propose two additional sliding pathways (three in total) between helices H2–H3 and H6–H1, ending at the triplet arginines R84 and R277 in the protein cavity. Initial binding on the matrix side and electrophysiological measurements show that the pathway between helices H6 and H1 terminating at R277 does not function, possibly because H6–H1 are terminal helices with two negatively charged residues on the matrix side (E262 and E46) that are repulsive to the FA anion. All residues involved in the sliding pathway are conserved in the other proteins of the family (UCP2-5, ANT1, and OGC). We believe that the mechanism can be generalized to other members of the SLC25 superfamily.

3 | Materials and Methods

3.1 | MD Simulations Systems

Three main systems were simulated with UCP1 in the c-state, which is open to the cytoplasmic side:

1. UCP1 (AF-P12242-F1-v4) in 0.5 DOPC: 0.5 DOPE +3 bound CDL molecules—1 μs simulation,
2. UCP1 (AF-P12242-F1-v4) in 0.45 DOPC: 0.45 DOPE: 0.10 AA (50% in negative and 50% in neutral form) +3 bound CL molecules, 2 μs simulation,

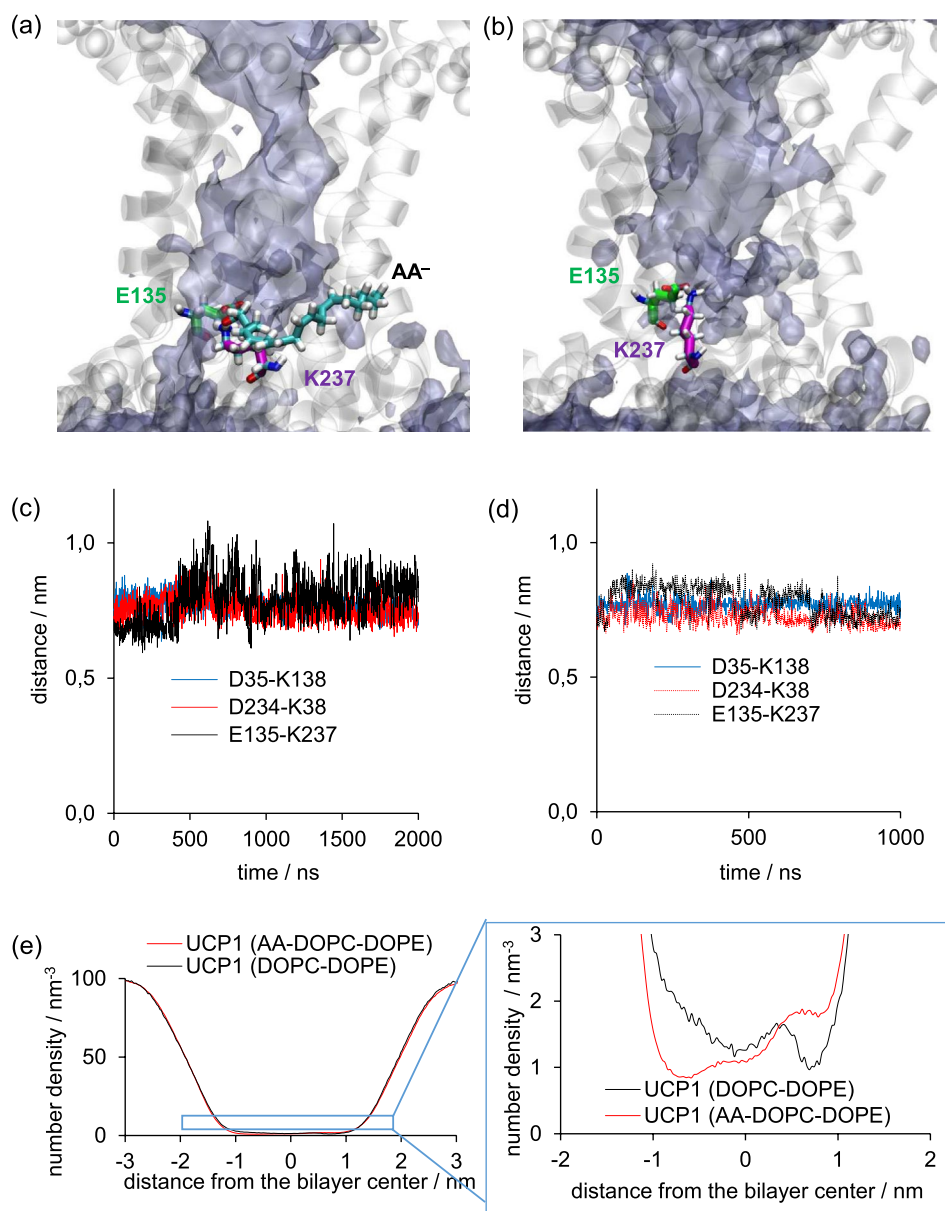


FIGURE 6 | UCP1 is impermeable to water. Average water density in (a) 2 μ s MD simulation of UCP1 with AA⁻ in the membrane (b) 1 μ s MD simulation of UCP1 without AA⁻ in the membrane. Distances of salt bridges connected in the salt bridge network for (c) 2 μ s MD simulation of UCP1 with AA⁻ (d) 1 μ s MD simulation of UCP1 without AA⁻ in the membrane. (e) Water number density along the bilayer in MD simulations of UCP1 with and without AA⁻.

3. UCP1 (AF-P12242-F1-v4) in 0.45 DOPC: 0.45 DOPE: 0.10 AA (50% in negative and 50% in neutral form) + 3 bound CL molecules—protonated sliding AA⁻ from simulation 2 at $t = 2000$ ns, 1 μ s simulation.

3.2 | Setup Used in MD Simulations

All simulation boxes contained UCP1 protein with a total charge of +15 based on the available mouse (*Mus musculus*) AlphaFold structure (AF-P12242-F1-v4) [30], 115 lipid molecules per leaflet (230 in total; 115 DOPC and 115 DOPE symmetrically distributed), three bound CL molecules on the matrix side of the protein (−2 charge each CL, TLCL2), and 130 molecules of water per lipid (~31 000 in total). The crystal structure of the ANT1 protein

(PDB code 1OKC) [33] served as a template for three binding CL molecules. Three binding CL positions are confirmed by the cryo-EM structure of the GTP-bound state of UCP1 (PDB code 8G8W) [29]. When 10% AA is present in the lipid bilayer, their initial position is in the upper and lower leaflet of the membrane (22 molecules in total, 11 neutral and 11 anionic forms). All systems were constructed using the CHARMM-GUI membrane builder input generator [36]. UCP1 was positioned in the membrane using the PPM 2.0 web server. Hydrogen atoms were added using CHARMM-GUI so that the side chains of all arginines and lysines were positively charged. Histidines (with hydrogen on epsilon nitrogen—HIE) and cysteines were prepared in their neutral form, while the side chains of glutamates and aspartates were deprotonated and negatively charged. Chloride/potassium ions were added to neutralize the systems.

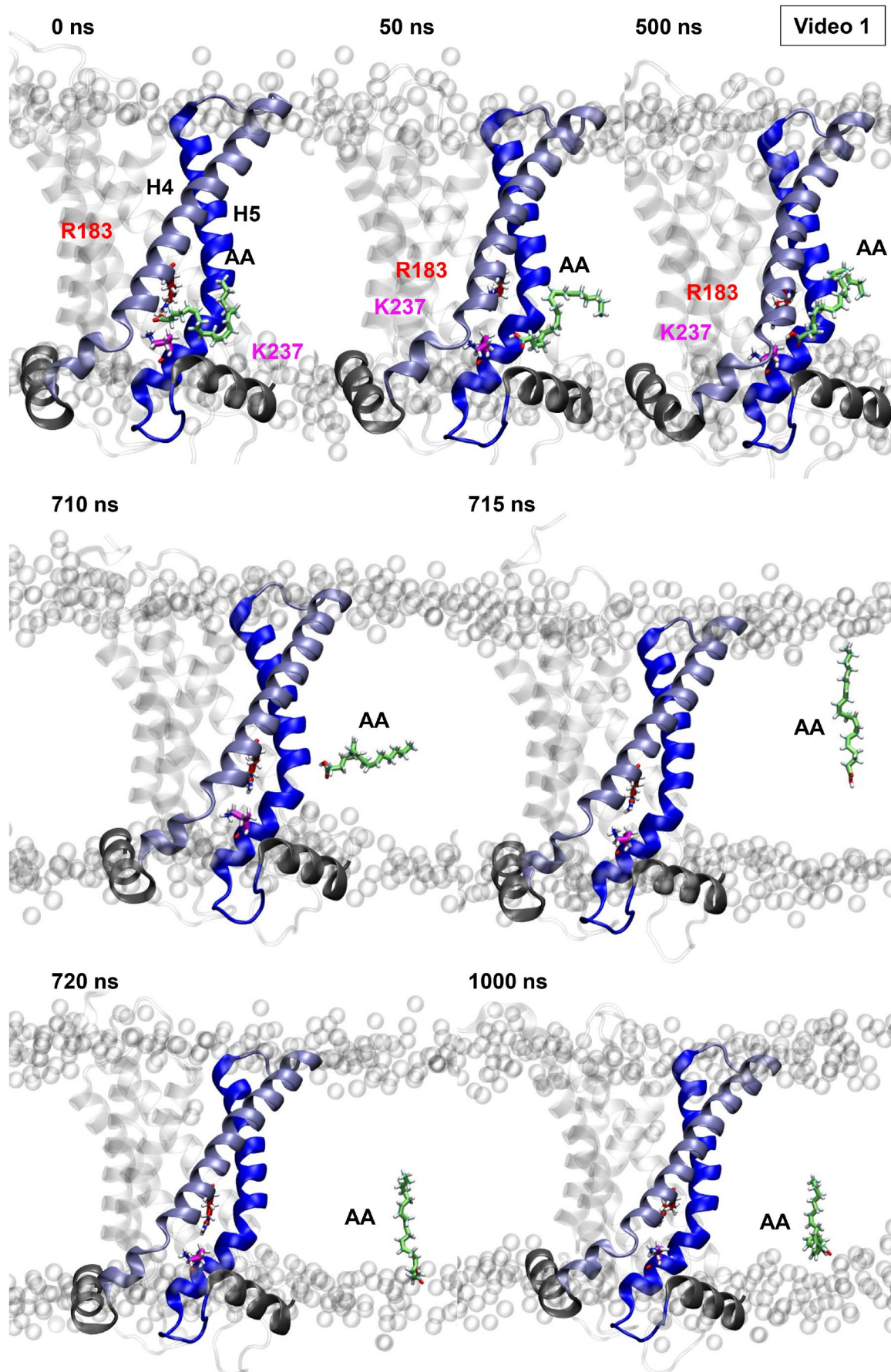


FIGURE 7 | Legend on next page.

FIGURE 7 | Protonation of AA⁻ results in its exit from the UCP1 binding site into the lipid bilayer. Time course of the 1 μ s simulation when AA⁻ is protonated (AA). AA is shown in green. 0 ns: The arachidonic acid anion (AA) is inside the UCP1 cavity. After sliding along the positively charged protein-lipid interface from K237, AA is now bound to R183. Protonation occurs. 50 and 500 ns: The protonated FA has already started moving out of UCP1 toward the membrane. The electrostatic interactions with R183 are weaker, allowing the exit phase. The FA appears close to the edge of the protein cavity, suggesting that it is being released into the bilayer. 710–715 ns: The FA has fully exited the protein and is now in the bilayer. At 715 ns, the FA is visible in the bilayer. The tail points to the cytosolic side of the bilayer. 720 ns: The FA is now directed toward the matrix side of the membrane. It no longer interacts with UCP1, confirming that the protein has facilitated its translocation. 1000 ns: The FA is positioned on the matrix side, where the lower pH will drive it to lose a proton. This deprotonation step is critical to restart the FA cycling mechanism. The now negatively charged FA anion can then be taken up by UCP1 for transport back. See also Video S1 in the Supplementary Results.

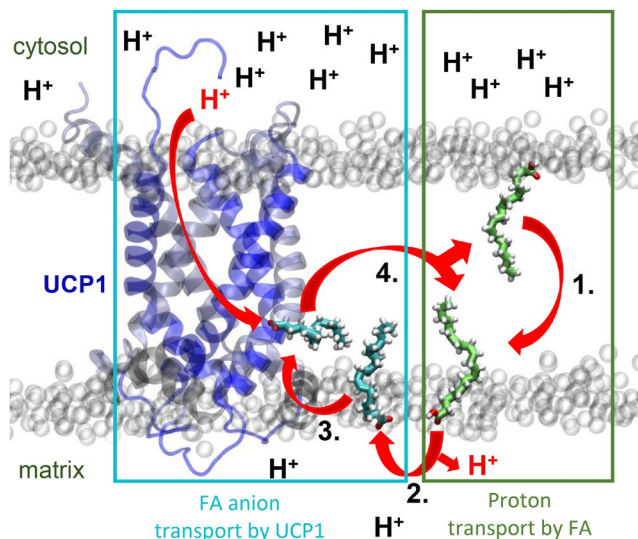


FIGURE 8 | Modification of the proton transport mechanism in UCP1 according to new MD simulation results together with membrane conductance experiments. Modified FA cyclic model, neutral FA is shown in green, while the anionic form of FA is shown in cyan. The model can be divided into four steps: 1. translocation of protonated FA across the bilayer from the cytosolic to the matrix side; 2. deprotonation of FA on the matrix side; 3. attraction of FA⁻ to the positively charged ring on the matrix side and sliding toward the cytosolic side; 4. protonation of FA anion and release of protonated FA, which can be toward the matrix or cytosolic side of the bilayer. If it is toward the matrix side of the bilayer, the first step in the cycle is skipped and the entire cycle is shortened by one step.

Simulations were performed using Gromacs2022 and the CHARMM36m force field with periodic boundary conditions (PBC) in all directions [37–41] with a cubic box filled with the TIP3P model of water molecules. All systems were first minimized and equilibrated using the CHARMM-GUI protocol [36] with the geometry first optimized in 1000 cycles and then equilibrated for 10 ns in the equilibration process provided by the CHARMM-GUI solution builder module, with different restraints being subsequently applied [42]. The production phase lasted for one or two μ s, depending on the system without any constraints with a 2 fs time step in a periodic rectangular box of 9.5 nm \times 9.5 nm \times 14.4 nm. The isobaric-isothermal ensemble (NPT) at T = 310 K was maintained by a Nosé–Hoover thermostat [43] independently for the membrane, protein, and water/ion subsystems with a coupling constant of 1.0 ps⁻¹. The pressure was set at 1.013 bar and controlled by a semi-isotropic Parrinello–Rahman barostat [44] with a pressure coupling time constant of 5 ps⁻¹. Long-range electrostatics were calculated using the particle-mesh Ewald (PME) method [45, 46]

with real space Coulomb interactions cut off at 1.2 nm using a Fourier spacing of 0.12 nm and a Verlet cut-off scheme.

3.3 | Trajectory Analysis

We used the Gromacs tool for analysis and VMD for visualization [47]. Unless otherwise noted, distances were calculated as the distance from the residue center of mass.

3.4 | Calculation of the Electrostatic Potential

The electrostatic potential was calculated using the PMEpot plugin in VMD [48] for each frame of the whole system (protein, water, lipids, AA, counterions) and then averaged over the entire trajectory. The potential was projected in the range of -2 to +2 eV.

3.5 | Chemicals

Sodium sulfate (Na₂SO₄), 2-(N-morpholino)ethanesulfonic acid (MES), tris(hydroxymethyl)-aminomethane (Tris), sodium dodecyl sulfate (SDS) ethylene glycol-bis(β -aminoethyl ether)-N,N,N',N'-tetraacetic acid (EGTA) were purchased from Carl Roth GmbH & Co. K.G. (Karlsruhe, Germany). Hexane, hexadecane, adenosine 5'-triphosphate (ATP), guanosine 5'-triphosphate (GTP), and agarose were purchased from Sigma-Aldrich Co. (Vienna, Austria). 1,2-dioleoyl-sn-glycero-3-phosphocholine (DOPC), 1,2-dioleoyl-sn-glycero-3-phosphoethanolamine (DOPE), and CL were purchased from Avanti Polar Lipids Inc. (Alabaster AL, USA) and chloroform—from Sanova Pharma GesmbH (Austria). Arachidonic acid (AA) was purchased from Larodan (Biozol, Eching, Germany).

3.6 | Cloning, Site-Directed Mutagenesis, Isolation, and Reconstitution of Murine UCP1

Cloning, isolation, and reconstitution of murine UCP1 and UCP1 mutants followed an established protocol [49]. In brief, pET24a expression plasmids containing selected cDNA sequences were transformed into *E. coli* Rosetta DE3 strain (Novagen, Darmstadt, Germany). Inclusion bodies (IBs) were isolated by centrifugation of cells disrupted by a high-pressure cell disruptor (One Shot, Constant Systems Ltd., Daventry, UK) at 1 kbar. For re-folding, purification, and reconstitution, the protein was first

(a)

		H1	
UCP1	-----MVNPT-----TSEVQPTMGVKIFSAGVSACLADIITFE	33	
UCP2	-----MVGFK-----ATDVPPTATVKFLGAGTAACIADLITFE	33	
UCP3	-----MVGLQ-----PSEVPPTTVVKFLGAGTAACFADLLTFF	33	
UCP4	-----MPIAEEEEKLLPLTQRWPRTSKFLLSGCAATVAELATFE	38	
UCP5	MGIFPGIILIFLRVKFATAAIVSGHQKSTLSHEMSGLNWKPFVYGGLASIVAEGFTFE	60	
ANT1	-----MGDQALSFLKDFLAGGIAAAVSKTAVAF	28	
OGC	-----MAATASPGAG--RMDGKPRTSPKSVKFLFGGLAGMGATVFVQF	41	
	— H1 —	h1 — H2 —	
UCP1	LD TAK VRLQIQGEGQA-----SSTIRYKGVLTITTLAKTEGLPKLYSGLPAGIQ RQ I	86	
UCP2	LD TAK VRLQIQGESQGLV---RTAASAQYRGVLGTILTMVRTEGPRSLYNGLVAGLQ RQ M	90	
UCP3	LD TAK VRLQIQGENPG-----AQSVQYRGVLGTILTMVRTEGPRSPYSGLVAGL HRQ M	86	
UCP4	LDLT K TRLQMGEAALARLGDGAVDSAPYRGMVRTALGIVQEEGFLKLWQGVTPAIY R HV	98	
UCP5	VDLT K TRLQVQGSIDV-----RFKEIKYRGMFHALFRIYKEEGILALYSGIAPALL RQ A	115	
ANT1	IERV K LLLVQHASKQI-----SAEKQYKGIIDCVVRIPKEQGFLSFWRGNLANV RY F	82	
OGC	LDLV K NRMQLSGEGAK-----TREYKTSFHALTSILKTEGLKGIYTGLSAGLL RQ A	92	
	— H2 —	H3 — H4 —	
UCP1	SFASLRIGLYDSVQEYFSSGRE-TPASLGNKISA---GLMTGGVAVFIGQ PTE VV K VRM	141	
UCP2	SFASVRIGLYDSVKQFYT-KGS-EHAGIGSRLLA---GSTTGALAVAVAQ PTE DVV K VRM	144	
UCP3	SFASIRIGLYDSVKQFYTPKA-DHSSVAIRILA---GCTTGAMAVTCAQ PTE DVV K VRM	141	
UCP4	VYSGGRMVTYEHLREVVFVKSEDKHYPLWKSIVG---GMMAGVIGQFLAN PTE DLV K VQM	154	
UCP5	SYGTIKIGIYQSLKRLFVERLE--DETLLINMIC---GVVSGVISSTIAN PTE DLV K IRM	169	
ANT1	PTQALNFAFKDKYKQIFLGGVD-RHKQFWRYFAGNLASGGAAGATSLCFVY PTE DFAR TR L	141	
OGC	TYTTTRLGIYTVLFERLTGADG-TPPGFLLKALI---GMTAGATGAFVGT PAE VAL IR M	147	
	H3 — h2 —	H4 — h3 —	
UCP1	QAQSHLH--GIKPRYTGTYNAYRVIATTESLSTLWKGTTPNLM R NVIINCTELVTYDLMK	199	
UCP2	QAQARA---GGRRYQSTVEAYKTIAREEGIRGLWKGTSPNVA R NAIVNCAELVTYDLIK	201	
UCP3	QAMIRLG-TGGERKYRGTMDAYRTIAREEGVRGLWKGTWPNIT R NAIVNCAEMVTYDIK	200	
UCP4	QMEGKRRLEKPLRFRGVHHAFAKILAEGGIRGLWAGWIPNIQ R AALVNMGDLTTYDTVK	214	
UCP5	QAQGSFL-QG-----SMIGSFIDYQQEGTRGLWRGVVPTAQ R AAIVVGVELPVYDITK	222	
ANT1	AADVKGK--SSQREFNGLGDCLTKIFKSDGLKGLYQGFVSQVQGI IYRAAYFGVYDTAK	199	
OGC	TADGRLP-ADQRRGYKNVFNALVRIAREEGVPTLWRGCIPTMA R AVVNVNAAQLASYSQSK	206	
	H4 — H5 — h3		
UCP1	GALVNNKILADDVPCHLLSALVAGFCTTLLAS FVD V K TRFINSL-----PGQYPSVPS	253	
UCP2	DTLLKANLMTDDLPCFHTSAFGAGFCTTVIAS FVD V K TRYMNSA-----LGQYHSAGH	255	
UCP3	EKLLESHLFTDNFPCHFVSFAFGAGFCATVVAS FVD V K TRYMNAP-----LGRYRSLPH	254	
UCP4	HYLVNLNTPLEDNISTHGLSSLCGLVASILGTP ADV I K SRIMNQPRDKQGRGLLYKSSAD	274	
UCP5	KHLIVSGMLGDTILTHFVSSFTCGLAGALASN FVD V K TRMMNQRAIV-GHVDLYKGTLD	281	
ANT1	GMLPDPKNVH--IIVSWMIAQSVTAVAGLVSY PFD T V RRMMMQSGRK-GADIMYTGTL	256	
OGC	QFLLDSGYFSDNILCHFCASMISGLVTTAAS FVD I V KTRIQNMRMID-G-KPEYKNGLD	264	
	— h3 —	H6	
UCP1	CAMSMYTKEGPTAFFKGFVASFL RL GSWNVIMFVCFEQLKELMKSRQTVDC	307	
UCP2	CALTMLRKEGPRAFYKGFMP SFL RL GSWNVVMFVTYEQLKRALMAAYQSREAP	309	
UCP3	CMLKMVAQEGPTAFYKGFV SFL RL GAWNVMMFVTYEQLKRALMKVQVLR SPF	308	
UCP4	CLIQAVQGEGLSLYKGF LPS WL RM TPWMSVFWLTYEKIREMSGVS-----PF	322	
UCP5	GILKMWKHEGFFALYKGF PN WL RL GPWNIFFITYEQLKRLQI-----	325	
ANT1	CWRKIAKDEGANAFFKGAWSNV LR GMGG-AFVLVLYDEIKKYV-----	298	
OGC	VLLKVRYEGFSLWKGF TP Y AR LGPHTVLTFIFLEQMNKAYKRLFLSG----	314	

(b)

% Identity	UCP1					
UCP2	57	UCP2				
UCP3	54	75	UCP3			
UCP4	30	34	35	UCP4		
UCP5	33	37	39	37	UCP5	
ANT1	20	23	23	23	26	ANT1
OGC	31	33	33	30	37	21

FIGURE 9 | Legend on next page.

FIGURE 9 | Generalization of the sliding mechanism within other SLC25 family proteins. (a) Alignment of mouse UCP1 with other mouse uncoupling proteins (UCPs), oxoglutarate protein (OGC), and ANT1 protein, which show increased conductance in the presence of protein and FA. The positions of completely identical amino acids are marked with an asterisk (*), the positions of amino acids with high similarity are marked with a colon (:), and the positions of amino acids that are similar are marked with a dot (.). Conserved salt bridge network amino acids on the matrix side (c-state configuration of the protein) are colored green (positively charged) and purple (negatively charged). The final sliding points, the arginine triplet, are well conserved among all proteins and are colored in red. Other conserved motifs are also highlighted in different colors—proline kicks in dark green, and EG motifs in gray. (b) Table of identity between primary sequence alignment of mouse UCP1 with other uncoupling proteins (UCP2-5), 2-oxoglutarate protein (OGC), and ANT1 protein.

solubilized in 100mM Tris at pH7.5, 5mM EDTA, 10% glycerin (TE/G-buffer) containing 2% sodium lauryl sulfate and 1mM DTT. Membrane-forming lipids (DOPC, DOPE, and CL; 45:45:10mol%) dissolved in TE/G-buffer containing 1.3% Triton X-114, 0.3% n-octylpolyoxyethylene, 1mM DTT, and 2mM GTP were gradually mixed with proteins. The mixture was concentrated and dialyzed against the buffer used in the experiments (50mM Na₂SO₄, 10mM MES, 10mM Tris, and 0.6mM EGTA at pH7.34). Unfolded and aggregated proteins were removed from the dialysate by centrifugation and passage through a hydroxyapatite column. Non-ionic detergents were removed by application of Bio-Beads SM-2 (Bio-Rad Laboratories, Hercules, CA, USA). Protein concentration in proteoliposomes was measured using the Micro BCA Protein Assay Kit (Thermo Fisher Scientific, Waltham, MA, USA). Protein purity was verified by SDS-PAGE and silver staining.

To generate UCP1 mutants, site-directed mutagenesis of R84, R183, R277, and the double mutation R84/R183 to serine was performed using the Q5 Site-Directed Mutagenesis Kit (New England Biolabs, Austria). Sequences were verified by both DNA and amino acid sequencing. Mutants were always refolded in parallel with a wild type to minimize artifacts. In addition, we performed control measurements by activating the mutant and the wild-type protein refolded in parallel by free FA and inhibiting by 4mM ATP to test protein functionality.

3.7 | Measurements of Membrane Conductance in Planar Lipid Bilayer Membranes

Planar lipid bilayers were formed at the tip of the dispensable plastic pipette as described [50]. Proper membrane formation was verified by membrane capacitance measurements ($C = 0.71 \pm 0.03 \mu\text{F}/\text{cm}^2$). C was independent of the presence of protein, AA, and inhibitor. Current-voltage (I-U) recordings were taken with a patch-clamp amplifier (EPC 10, HEKA Elektronik, Dr. Schulze GmbH, Lambrecht, Germany).

Total specific membrane conductance (G_m) at 0mV was obtained as the slope of a linear fit of the experimental data at the applied voltages from -50mV to +50mV, normalized to the membrane area. AA dissolved in chloroform and ATP dissolved in assay buffer (pH=7.34) were added to the membrane-forming lipid solution. Substrate concentrations are indicated in the figure legends.

3.8 | Multiple Sequence Alignment

Multiple sequence alignment was performed on the mouse proteins ANT1, UCP1-5, and OGC using the online tool from

UniProt (“UniProt: the Universal Protein Knowledgebase in 2023 The UniProt Consortium,” 2022).

3.9 | Statistical Analysis

Statistical analyses were performed using Sigma Plot 12.5 (Systat Software GmbH, Erkrath, Germany). Data from the electrophysiological experiments are represented as mean \pm standard deviation of at least three technical replicates performed on three different days. Each technical replicate was the mean conductance of three to ten lipid bilayer membranes formed on the same day.

Author Contributions

Sanja Vojvodić: investigation, writing – original draft, validation, visualization, methodology, writing – review and editing, formal analysis. **Giorgia Roticiiani:** investigation, writing – review and editing, visualization, validation, formal analysis. **Mario Vazdar:** writing – review and editing, methodology, supervision, funding acquisition. **Elena E. Pohl:** conceptualization, funding acquisition, writing – original draft, writing – review and editing, project administration, supervision, resources.

Acknowledgments

We are grateful to Dr. Olga Jovanović for valuable discussions and Sarah Bardakji, MSc. for the excellent technical assistance. Open access funding provided by Veterinarmedizinische Universität Wien/KEMÖ.

Conflicts of Interest

The authors declare no conflicts of interest.

Data Availability Statement

The data that support the findings of this study are available from the corresponding author upon reasonable request.

References

1. P. Mitchell, “Coupling of Phosphorylation to Electron and Hydrogen Transfer by a Chemi-Osmotic Type of Mechanism,” *Nature* 191 (1961): 144–148, <https://doi.org/10.1038/191144a0>.
2. M. D. Brand, “The Proton Leak Across the Mitochondrial Inner Membrane,” *Biochimica et Biophysica Acta* 1018 (1990): 128–133, [https://doi.org/10.1016/0005-2728\(90\)90232-s](https://doi.org/10.1016/0005-2728(90)90232-s).
3. D. Ricquier and F. Bouillaud, “Mitochondrial Uncoupling Proteins: From Mitochondria to the Regulation of Energy Balance,” *Journal of Physiology* 529, no. Pt 1 (2000): 3–10, <https://doi.org/10.1111/j.1469-7793.2000.00003.x>.
4. A. Andreyev, T. O. Bondareva, V. I. Dedukhova, et al., “The ATP/ADP-Antiporter Is Involved in the Uncoupling Effect of Fatty Acids on

- Mitochondria,” *European Journal of Biochemistry* 182 (1989): 585–592, <https://doi.org/10.1111/j.1432-1033.1989.tb14867.x>.
5. J. Kreiter, A. Rupprecht, S. Škulj, et al., “ANT1 Activation and Inhibition Patterns Support the Fatty Acid Cycling Mechanism for Proton Transport,” *International Journal of Molecular Sciences* 22 (2021): 2490, <https://doi.org/10.3390/ijms22052490>.
 6. E. E. Pohl, A. Rupprecht, G. Macher, and K. E. Hilse, “Important Trends in UCP3 Investigation,” *Frontiers in Physiology* 10 (2019): 470, <https://doi.org/10.3389/fphys.2019.00470>.
 7. K. Zuna, T. Tyschuk, T. Beikbaghban, et al., “The 2-Oxoglutarate/Malate Carrier Extends the Family of Mitochondrial Carriers Capable of Fatty Acid and 2,4-Dinitrophenol-Activated Proton Transport,” *Acta Physiologica (Oxford, England)* 240 (2024): e14143, <https://doi.org/10.1111/apha.14143>.
 8. D. Ricquier, “UCP1, the Mitochondrial Uncoupling Protein of Brown Adipocyte: A Personal Contribution and a Historical Perspective,” *Biochimie* 134 (2017): 3–8, <https://doi.org/10.1016/j.biochi.2016.10.018>.
 9. D. G. Nicholls and E. Rial, “A History of the First Uncoupling Protein, UCP1,” *Journal of Bioenergetics and Biomembranes* 31 (1999): 399–406, <https://doi.org/10.1023/a:1005436121005>.
 10. B. Cannon, A. Hedin, and J. Nedergaard, “Exclusive Occurrence of Thermogenin Antigen in Brown Adipose Tissue,” *FEBS Letters* 150 (1982): 129–132, [https://doi.org/10.1016/0014-5793\(82\)81319-7](https://doi.org/10.1016/0014-5793(82)81319-7).
 11. D. G. Nicholls, “A History of UCP1,” *Biochemical Society Transactions* 29 (2001): 751–755, <https://doi.org/10.1042/bst0290751>.
 12. I. G. Shabalina, A. Jacobsson, B. Cannon, and J. Nedergaard, “Native UCP1 Displays Simple Competitive Kinetics Between the Regulators Purine Nucleotides and Fatty Acids,” *Journal of Biological Chemistry* 279 (2004): 38236–38248, <https://doi.org/10.1074/jbc.M402375200>.
 13. A. Fedorenko, P. V. Lishko, and Y. Kirichok, “Mechanism of Fatty-Acid-Dependent UCP1 Uncoupling in Brown Fat Mitochondria,” *Cell* 151 (2012): 400–413, <https://doi.org/10.1016/j.cell.2012.09.010>.
 14. E. Urbankova, A. Voltchenko, P. Pohl, P. Jezek, and E. E. Pohl, “Transport Kinetics of Uncoupling Proteins. Analysis of UCP1 Reconstituted in Planar Lipid Bilayers,” *Journal of Biological Chemistry* 278 (2003): 32497–32500, <https://doi.org/10.1074/jbc.M303721200>.
 15. G. Macher, M. Koehler, A. Rupprecht, J. Kreiter, P. Hinterdorfer, and E. E. Pohl, “Inhibition of Mitochondrial UCP1 and UCP3 by Purine Nucleotides and Phosphate,” *Biochimica et Biophysica Acta - Biomembranes* 1860 (2018): 664–672, <https://doi.org/10.1016/j.bbame.2017.12.001>.
 16. M. Klingenberg, “UCP1 - A Sophisticated Energy Valve,” *Biochimie* 134 (2017): 19–27, <https://doi.org/10.1016/j.biochi.2016.10.012>.
 17. V. P. Skulachev, “Fatty Acid Circuit as a Physiological Mechanism of Uncoupling of Oxidative Phosphorylation,” *FEBS Letters* 294 (1991): 158–162, [https://doi.org/10.1016/0014-5793\(91\)80658-p](https://doi.org/10.1016/0014-5793(91)80658-p).
 18. K. D. Garlid, D. E. Orosz, M. Modriansky, S. Vassanelli, and P. Jezek, “On the Mechanism of Fatty Acid-Induced Proton Transport by Mitochondrial Uncoupling Protein,” *Journal of Biological Chemistry* 271 (1996): 2615–2620, <https://doi.org/10.1074/jbc.271.5.2615>.
 19. E. Winkler and M. Klingenberg, “Effect of Fatty Acids on H⁺ Transport Activity of the Reconstituted Uncoupling Protein,” *Journal of Biological Chemistry* 269 (1994): 2508–2515.
 20. M. Klingenberg, “Wanderings in Bioenergetics and Biomembranes,” *Biochimica et Biophysica Acta* 1797 (2010): 579–594, <https://doi.org/10.1016/j.bbabi.2010.02.012>.
 21. Y. Wang and E. Tajkhorshid, “Electrostatic Funneling of Substrate in Mitochondrial Inner Membrane Carriers,” *Proceedings of the National Academy of Sciences of the United States of America* 105 (2008): 9598–9603, <https://doi.org/10.1073/pnas.0801786105>.
 22. P. Jezek, D. E. Orosz, M. Modriansky, and K. D. Garlid, “Transport of Anions and Protons by the Mitochondrial Uncoupling Protein and Its Regulation by Nucleotides and Fatty-Acids - a New Look at Old Hypotheses,” *Journal of Biological Chemistry* 269 (1994): 26184–26190.
 23. S. Skulj and M. Vazdar, “Calculation of Apparent pKa Values of Saturated Fatty Acids With Different Lengths in DOPC Phospholipid Bilayers,” *Physical Chemistry Chemical Physics* 21 (2019): 10052–10060, <https://doi.org/10.1039/c9cp01204d>.
 24. A. A. Pashkovskaya, M. Vazdar, L. Zimmermann, O. Jovanovic, P. Pohl, and E. E. Pohl, “Mechanism of Long-Chain Free Fatty Acid Protonation at the Membrane-Water Interface,” *Biophysical Journal* 114 (2018): 2142–2151, <https://doi.org/10.1016/j.bpj.2018.04.011>.
 25. F. Kamp, D. Zakim, F. Zhang, N. Noy, and J. A. Hamilton, “Fatty Acid Flip-Flop in Phospholipid Bilayers Is Extremely Fast,” *Biochemistry* 34 (1995): 11928–11937, <https://doi.org/10.1021/bi00037a034>.
 26. J. Kreiter, S. Škulj, Z. Brkljača, S. Bardakji, M. Vazdar, and E. E. Pohl, “FA Sliding as the Mechanism for the ANT1-Mediated Fatty Acid Anion Transport in Lipid Bilayers,” *International Journal of Molecular Sciences* 24 (2023): 13701, <https://doi.org/10.3390/ijms241813701>.
 27. J. Kreiter, T. Tyschuk, and E. E. Pohl, “Uncoupling Protein 3 Catalyzes the Exchange of C4 Metabolites Similar to UCP2,” *Biomolecules* 14 (2023): 21, <https://doi.org/10.3390/biom14010021>.
 28. Y. Kang and L. Chen, “Structural Basis for the Binding of DNP and Purine Nucleotides Onto UCP1,” *Nature* 620 (2023): 226–231, <https://doi.org/10.1038/s41586-023-06332-w>.
 29. S. A. Jones, P. Gogoi, J. J. Ruprecht, et al., “Structural Basis of Purine Nucleotide Inhibition of Human Uncoupling Protein 1,” *Science Advances* 9 (2023): eadh4251, <https://doi.org/10.1126/sciadv.adh4251>.
 30. J. Jumper, R. Evans, A. Pritzel, et al., “Highly Accurate Protein Structure Prediction With AlphaFold,” *Nature* 596 (2021): 583–589, <https://doi.org/10.1038/s41586-021-03819-2>.
 31. O. Jovanovic, K. Chekashkina, S. Skulj, et al., “Membrane Lipid Reshaping Underlies Oxidative Stress Sensing by the Mitochondrial Proteins UCP1 and ANT1,” *Antioxidants (Basel)* 11 (2022): 2314, <https://doi.org/10.3390/antiox11122314>.
 32. N. Senoo, D. K. Chinthapalli, M. G. Baile, et al., “Functional Diversity Among Cardiolipin Binding Sites on the Mitochondrial ADP/ATP Carrier,” *EMBO Journal* 43 (2024): 2979–3008, <https://doi.org/10.1038/s44318-024-00132-2>.
 33. E. Pebay-Peyroula, C. Dahout-Gonzalez, R. Kahn, V. Trézéguet, G. J. M. Lauquin, and G. Brandolin, “Structure of Mitochondrial ADP/ATP Carrier in Complex With Carboxyatractyloside,” *Nature* 426 (2003): 39–44, <https://doi.org/10.1038/nature02056>.
 34. L. Zhao, S. Wang, Q. Zhu, et al., “Specific Interaction of the Human Mitochondrial Uncoupling Protein 1 With Free Long-Chain Fatty Acid,” *Structure* 25 (2017): 1371–1379, <https://doi.org/10.1016/j.str.2017.07.005>.
 35. V. Beck, M. Jaburek, T. Demina, et al., “Polyunsaturated Fatty Acids Activate Human Uncoupling Proteins 1 and 2 in Planar Lipid Bilayers,” *FASEB Journal* 21 (2007): 1137–1144, <https://doi.org/10.1096/fj.06-7489com>.
 36. J. Lee, X. Cheng, J. M. Swails, et al., “CHARMM-GUI Input Generator for NAMD, GROMACS, AMBER, OpenMM, and CHARMM/OpenMM Simulations Using the CHARMM36 Additive Force Field,” *Journal of Chemical Theory and Computation* 12 (2016): 405–413, <https://doi.org/10.1021/acs.jctc.5b00935>.
 37. S. Jo, T. Kim, V. G. Iyer, and W. Im, “CHARMM-GUI: A Web-Based Graphical User Interface for CHARMM,” *Journal of Computational Chemistry* 29 (2008): 1859–1865, <https://doi.org/10.1002/jcc.20945>.
 38. S. Jo, J. B. Lim, J. B. Klauda, and W. Im, “CHARMM-GUI Membrane Builder for Mixed Bilayers and Its Application to Yeast Membranes,”

Biophysical Journal 97 (2009): 50–58, <https://doi.org/10.1016/j.bpj.2009.04.013>.

39. E. L. Wu, X. Cheng, S. Jo, et al., “CHARMM-GUI Membrane Builder Toward Realistic Biological Membrane Simulations,” *Journal of Computational Chemistry* 35 (2014): 1997–2004, <https://doi.org/10.1002/jcc.23702>.

40. M. J. Abraham, T. Murtola, R. Schulz, et al., “GROMACS: High Performance Molecular Simulations Through Multi-Level Parallelism From Laptops to Supercomputers,” *SoftwareX* 1-2 (2015): 19–25, <https://doi.org/10.1016/j.softx.2015.06.001>.

41. J. Huang, S. Rauscher, G. Nawrocki, et al., “CHARMM36m: An Improved Force Field for Folded and Intrinsically Disordered Proteins,” *Nature Methods* 14 (2017): 71–73, <https://doi.org/10.1038/nmeth.4067>.

42. S. Jo, T. Kim, and W. Im, “Automated Builder and Database of Protein/Membrane Complexes for Molecular Dynamics Simulations,” *PLoS One* 2 (2007): e880, <https://doi.org/10.1371/journal.pone.0000880>.

43. S. Nosé, “A Molecular Dynamics Method for Simulations in the Canonical Ensemble,” *Molecular Physics* 52 (1984): 255–268, <https://doi.org/10.1080/00268978400101201>.

44. M. Parrinello and A. Rahman, “Polymorphic Transitions in Single Crystals: A New Molecular Dynamics Method,” *Journal of Applied Physics* 52 (1981): 7182–7190, <https://doi.org/10.1063/1.328693>.

45. U. Essmann, L. Perera, M. L. Berkowitz, T. Darden, H. Lee, and L. G. Pedersen, “A Smooth Particle Mesh Ewald Method,” *Journal of Chemical Physics* 103 (1995): 8577–8593, <https://doi.org/10.1063/1.470117>.

46. P. F. Batcho, D. A. Case, and T. Schlick, “Optimized Particle-Mesh Ewald/Multiple-Time Step Integration for Molecular Dynamics Simulations,” *Journal of Chemical Physics* 115 (2001): 4003–4018, <https://doi.org/10.1063/1.1389854>.

47. W. Humphrey, A. Dalke, and K. Schulten, “VMD: Visual Molecular Dynamics,” *Journal of Molecular Graphics* 14, no. 33–38 (1996): 27–38, [https://doi.org/10.1016/0263-7855\(96\)00018-5](https://doi.org/10.1016/0263-7855(96)00018-5).

48. A. Aksimentiev and K. Schulten, “Imaging Alpha-Hemolysin With Molecular Dynamics: Ionic Conductance, Osmotic Permeability, and the Electrostatic Potential Map,” *Biophysical Journal* 88 (2005): 3745–3761, <https://doi.org/10.1529/biophysj.104.058727>.

49. K. Zuna, O. Jovanovic, L. S. Khailova, et al., “Mitochondrial Uncoupling Proteins (UCP1-UCP3) and Adenine Nucleotide Translocase (ANT1) Enhance the Protonophoric Action of 2,4-Dinitrophenol in Mitochondria and Planar Bilayer Membranes,” *Biomolecules* 11 (2021): 1178, <https://doi.org/10.3390/biom11081178>.

50. V. Beck, M. Jabůrek, E. P. Breen, R. K. Porter, P. Ježek, and E. E. Pohl, “A New Automated Technique for the Reconstitution of Hydrophobic Proteins Into Planar Bilayer Membranes. Studies of Human Recombinant Uncoupling Protein 1,” *Biochimica et Biophysica Acta* 1757 (2006): 474–479, <https://doi.org/10.1016/j.bbabi.2006.03.006>.

Supporting Information

Additional supporting information can be found online in the Supporting Information section.